applied sciences

MDPI

Article

Influence of Low-Temperature Stress-Relieving Treatment in the Fatigue Life of Components Produced by Laser Powder Bed Fusion in AlSi10Mg

Malcolm António [1], Rui Fernandes [1], Joel de Jesus [1,2,*], Luís Borrego [1,3], Ricardo Branco [1], José da Costa [1] and José Ferreira [1]

[1] CEMMPRE, ARISE, Department of Mechanical Engineering, University of Coimbra, Rua Luís Reis Santos, 3030-788 Coimbra, Portugal; uc2022129512@student.uc.pt (M.A.); uc2020158278@student.uc.pt (R.F.); borrego@isec.pt (L.B.); ricardo.branco@dem.uc.pt (R.B.); jose.domingos@dem.uc.pt (J.d.C.); martins.ferreira@dem.uc.pt (J.F.)
[2] UnIRE, ISEL, Department of Mechanical Engineering, Polytechnic University of Lisbon, Rua Conselheiro Emídio Navarro 1, 1959-007 Lisbon, Portugal
[3] Coimbra Institute of Engineering, Polytechnic University of Coimbra, Rua Pedro Nunes, 3030-199 Coimbra, Portugal
* Correspondence: joel.jesus@uc.pt

Abstract: This study investigates the impact of low-temperature stress-relieving treatment on the fatigue life of AlSi10Mg components produced by Laser Powder Bed Fusion (L-PBF). The research focuses on a bicycle crank arm, comparing its performance in as-built and heat-treated conditions. The heat treatment involved stress-relieving at 250 °C for 2 h, followed by water quenching. The study found that the as-built condition exhibited a supersaturated Si cellular-dendritic microstructure, while the heat-treated condition showed coarsening of β-Mg_2Si phases and Si precipitates. This morphological change led to a decrease in hardness and an increase in ductility. Fatigue tests demonstrated that the heat-treated crank arms achieved the target of 100,000 cycles without failure, unlike the as-built samples, which failed prematurely. The fractography analysis identified surface porosity as the primary crack initiation site. The findings suggest that low-temperature stress-relieving treatment can enhance the fatigue performance of L-PBF AlSi10Mg components by reducing residual stresses and improving defect tolerance.

Keywords: L-PBF; heat treatment; fatigue; aluminum alloy; laser additive manufacturing; stress relief

check for updates

Academic Editors: Giuseppe Lacidogna and Andrea Carpinteri

Received: 13 November 2024
Revised: 18 December 2024
Accepted: 24 December 2024
Published: 27 December 2024

Citation: António, M.; Fernandes, R.; Jesus, J.d.; Borrego, L.; Branco, R.; Costa, J.d.; Ferreira, J. Influence of Low-Temperature Stress-Relieving Treatment in the Fatigue Life of Components Produced by Laser Powder Bed Fusion in AlSi10Mg. *Appl. Sci.* **2025**, *15*, 112. https://doi.org/10.3390/app15010112

Copyright: © 2024 by the authors. Licensee MDPI, Basel, Switzerland. This article is an open access article distributed under the terms and conditions of the Creative Commons Attribution (CC BY) license (https://creativecommons.org/licenses/by/4.0/).

1. Introduction

Additive manufacturing (AM) has revolutionized the production of complex geometries and lightweight components in industries such as aerospace, automotive, and biomedical engineering. Among the various AM technologies, Laser Powder Bed Fusion (L-PBF) has emerged as a highly versatile method for producing high-performance metallic parts. L-PBF uses a laser to selectively melt and fuse powder particles layer by layer, enabling the fabrication of near-net-shaped components with reduced material waste and shorter production cycles. The L-PBF process has revolutionized the production of complex metallic parts [1].

AlSi10Mg, an aluminum alloy with good strength and heat resistance, is widely used in L-PBF, particularly in the automotive, aerospace, and engineering industries. The structural integrity of AlSi10Mg parts produced through L-PBF is critical, as these parts often face demanding operational conditions [2].

In the as-built condition, AlSi10Mg has a hierarchical microstructure where large Al grains present a fine cellular-dendritic solidification structure with submicron-sized primary Al cells and an intercellular Si network [3]. The microstructure of the AlSi10Mg alloy produced through L-PBF is distinguished by features arising from the rapid solidification and localized heating associated with the process. The high cooling rates result in a refined microstructure characterized by a fine distribution of silicon particles within the aluminum matrix. Typically, the alloy exhibits a cellular or dendritic structure, where aluminum-rich cells are surrounded by silicon-enriched boundaries. This rapid solidification also leads to a supersaturation of silicon in the aluminum matrix, which influences the material's mechanical properties. Furthermore, the process introduces residual stresses and specific crystallographic textures due to the localized heating and cooling cycles. While the as-built microstructure enhances the mechanical performance of AlSi10Mg, providing higher strength and ductility compared to cast alloys, it often requires post-processing, such as heat treatments, to alleviate residual stresses and homogenize the silicon particle distribution, ensuring optimal performance [4–6]. The T6 treatment is frequently investigated for this alloy involving a solution treatment followed by artificial aging. This process causes the reorganization of the Si phase, which changes from a nanoscale precipitate arranged in a cellular network to coarse Si particles several microns in size. As T6 has often been found to be detrimental to strength, other authors have investigated alternative heat treatment strategies such as direct aging/T5 [7,8].

Research has demonstrated that AlSi10Mg parts produced by L-PBF can exhibit variations in mechanical behavior based on processing parameters. Fatigue failure, especially in high-cycle regimes, is influenced by factors such as as-build orientation, surface defects, and internal porosity. Studies show that optimizing process parameters and post-treatments like heat treatment can improve the fracture resistance and durability of these components [9].

Components made from AlSi10Mg via L-PBF tend to have a unique microstructure that affects their mechanical performance. Heat treatments, such as annealing, can significantly alter this microstructure, influencing hardness, ductility, and fracture mechanisms. For example, an annealed AlSi10Mg part may exhibit different failure modes compared to a non-treated one, with improved fracture toughness in some cases [10].

This alloy has been widely used in prototype vehicle parts due to its good balance of strength and lightweight. However, real-world component failures are often related to the presence of residual stresses, which are introduced during the L-PBF process. Optimizing the laser parameters and applying appropriate post-processing strategies can mitigate these issues [11].

The presence of adverse residual stresses has a special impact on the fatigue phenomena. Fatigue is a process of progressive material degradation that occurs when a material is subjected to dynamic loadings. This degradation consists of the initiation and propagation of one or more cracks in parts subjected to dynamic stresses leading to their failure. Residual stresses interact with applied stresses by modifying the loading cycle. It can be said that residual stresses act as mean stress. For this reason, they interact with the mean stress of the applied stress cycle, thereby modifying the effective stress ratio, which can be detrimental to the fatigue life [12].

The main objective of this work is to prove, using a real functional part, the benefits of a heat treatment previously studied by the authors [9] on fatigue behavior. This treatment is similar to the concept of a traditional TS, also known as stress relief heat treatment, for aluminum alloys. The chosen functional part was a bicycle crank arm. Typically, the cranks are made from aluminum alloy and are subjected to different types of cyclic combined stress as tensile, torsional, and bending [13].

In this work, the analysis was conducted in two phases: first, the development of an improved crank design with various modifications aimed at reducing the weight produced by L-PBF from a conventional crank design. The second phase was to analyze the fatigue life in two different conditions: a crank arm subjected to stress-relieved heat treatment and an as-build condition.

2. Materials and Methods

In the initial phase, the simplest crank arm produced by a Portuguese bike manufacturer, Miranda® (Borralha, Portugal), was chosen as the basis for developing a new optimized model, featuring reduced weight and a more complex geometry, to be produced by L-PBF. Figure 1 shows the crank shape (exact dimensions cannot be disclosed).

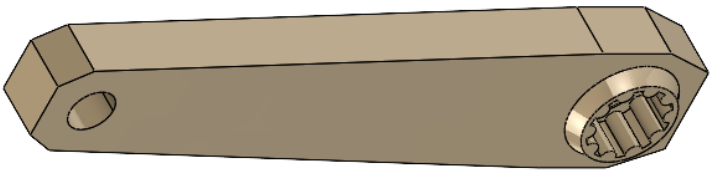

Figure 1. Crank with a simple shape, with a weight of 335 g.

These crank arms are produced through a forging process, followed by subtractive manufacturing to produce the splined shaft and the drilled hole. Table 1 presents the nominal chemical composition of the aluminum alloy 6061-T6. These crank arms have a mass of 335 g.

Table 1. Nominal chemical composition for AA 6061-T6 (wt.%) [14].

Al	Si	Mg	Mn	Cu	Fe	Zn	Ti	Others
Bal.	0.4–0.8	0.8–1.2	0–0.15	0.15–0.4	0–0.7	0–0.25	0–0.15	0–0.15

2.1. Topology Optimization Method

As mentioned previously, an improved crank arm design was developed from the conventional crank design detailed earlier. The topology optimization was performed using software such as Autodesk Inventor 2025® and Autodesk Inventor Nastran 2025®. In order to obtain a first approach, the Shape Generator tool from Autodesk Inventor was used. In the Shape Generator settings, Young's modulus was defined as 72 GPa, and the applied load was set to 1300 N at an angle of 45°, 65 mm from the crank arm's cross-sectional plane (yellow arrow in Figure 2a), as specified in the NP EN ISO 4210-8:2019 [15] standard for adults and youth leisure bicycles. Furthermore, two cylinders from the standard shape were preserved, as marked with black arrows in Figure 2a, and 206,691 tetrahedral elements were used to perform the Finite Element Analysis (FEA).

Figure 2b shows the result of the Shape Generator analysis, achieving a weight reduction of 51% in comparison with the standard model. The authors considered the mechanical properties presented in Table 2. These properties were obtained in previous work [9] under the same conditions as those to be examined in this work: an additively manufactured aluminum alloy, AlSi10Mg, in two conditions: as-built and heat-treated.

Using these mechanical properties and the data obtained from the Shape Generator tool, a new crank arm was designed through FEA in Autodesk Inventor Nastran. The FEA model was developed using a linear static analysis with 308,648 tetrahedral elements, resulting in a final shape that achieved a 26% weight reduction compared to the standard form. Figure 3 shows the FEA results for the final topology analyzed.

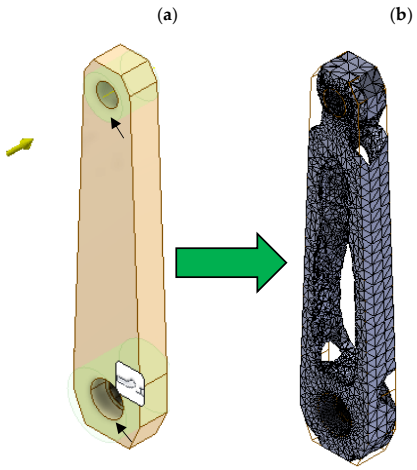

Figure 2. Topology optimization, (**a**) standard shape, and (**b**) result from the Shape Generator.

Table 2. Mechanical properties of the tested aluminum alloy [9].

Series	σ_{UTS} (MPa)	σ_{YS} (MPa)	εf (%)	E (GPa)
As-build	435	250	4.1	72
HT	380	210	5.6	72

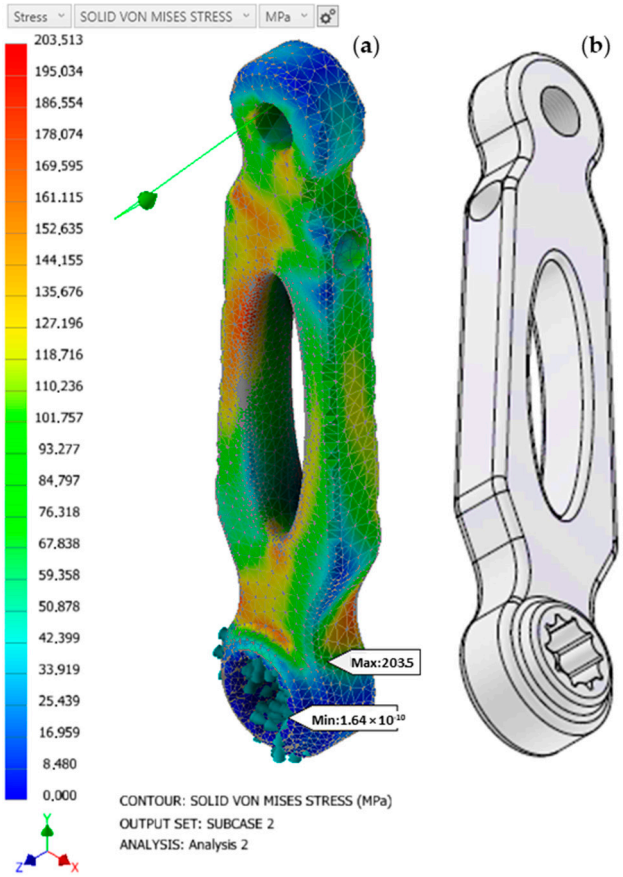

Figure 3. (**a**) FEA results and (**b**) final topology.

Observing the FEA results (Figure 3b), it can be concluded that the maximum Von Mises stress value was 203.51 MPa, which is clearly below the yield stress listed in Table 2.

2.2. Additive Manufacturing Process

After defining the final geometry, six crank arms were produced using the L-PBF process with AlSi10Mg using a Renishaw machine, AM 400 model (Technical Laboratory Systems, Inc., Katy, TX, USA). The main process parameters were a laser power of 350 W, a layer thickness of 30 µm, a scanning speed of 1.8 m/s, and a beam diameter of 70 µm. The nominal chemical composition of the AlSi10Mg aluminum alloy is summarized in Table 3. Figure 4 illustrates an as-build crank arm produced in this work. The relative density of the printed part was about 99.7%.

Table 3. Nominal chemical composition of the used aluminum alloy (wt.%) [16].

Al	Si	Mg	Mn	Cu	Fe	Zn	Ti	Ni	Pb	Sn
Bal.	9–11	0.25–0.145	0.45	0.05	0.55	0.10	0.15	0.05	0.05	0.05



Figure 4. Crank arm produced by L-PBF.

2.3. Post-Treatment Condition

Following the manufacture of the specimens, a post-processing heat treatment was applied to only three samples. The heat treatment consisted of a low-temperature stress relieving at 250 °C for 2 h, followed by water quenching. Additionally, the as-built state was also examined.

2.4. Microstructure and Hardness

Metallographic analyses were conducted on the cross-sections of each material condition to evaluate their morphological characteristics, adhering to the procedures recommended in the ASTM E3 standard [17]. The specimens were polished and etched with a modified Poulton's reagent to reveal the grain structure. Key microstructures were identified using scanning electron microscopy (SEM) with a Hitachi Jeol JSM-5310 model (Tokyo, Japan) using a current tension of 15 kV; this device also performed the EDS map.

Hardness tests were performed on each material condition using a fully automated hardness testing system, the Struers Type Duramin model (Copenhagen, Denmark). Random indentations were made on the specimens under a testing load of 100 g for 15 s, following the ASTM E384 standard [18].

2.5. Fatigue Tests and Fractography

The fatigue tests were performed on a test bench specifically developed for this purpose, based on the NP EN ISO 4210-8:2019 standard [15]. Figure 5a shows a real photograph of the test bench, and Figure 5b illustrates the standard suggestion.

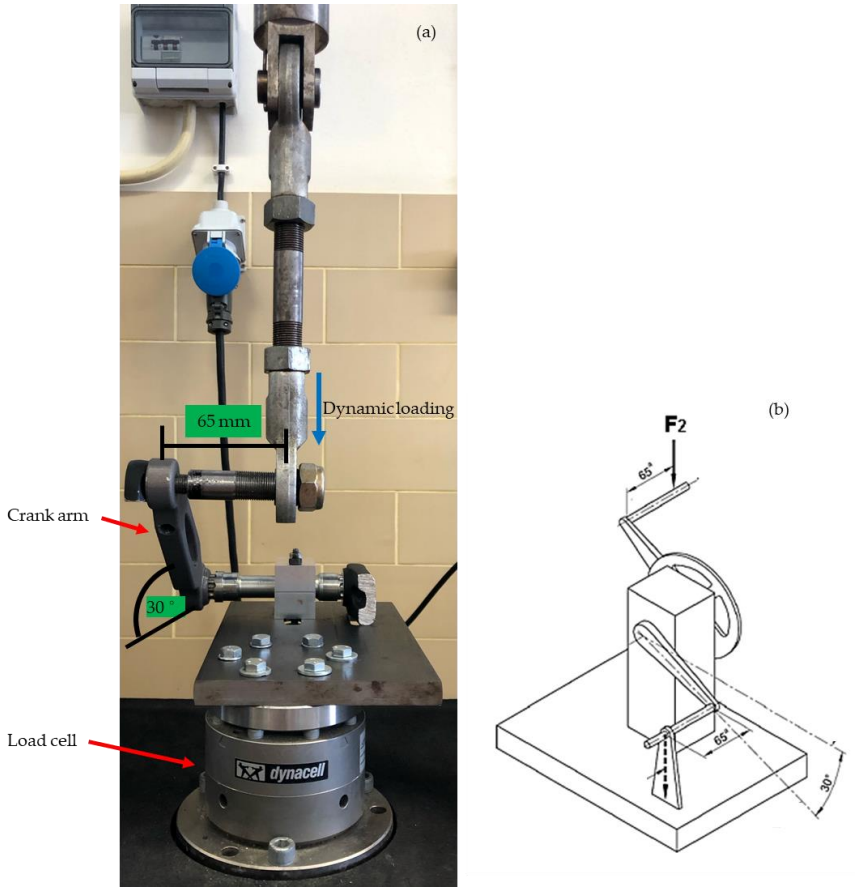

Figure 5. (**a**) Fatigue tests device and (**b**) NP EN ISO 4210-8:2019 standard proposal [15].

The NP EN ISO 4210-8:2019 standard [15] recommends testing the crank arm at an angle of 30° or 45°, with the load applied at 65 mm from the longitudinal plane of the crank arm, as can be observed in Figure 5a,b. This device was attached to a servo-electric testing machine, the model Instron ElectroPuls E10000 (Norwood, MA, USA). The fatigue tests were performed at room temperature under constant amplitude (R = 0) with sinusoidal load waves, and a cyclic frequency of 5 Hz. The objective of the fatigue tests was to comply with the recommendations of the NP EN ISO 4210-8:2019 standard for a youth and adult leisure bicycle, specifying a fatigue life of 100,000 cycles with 1300 N of maximum load.

Additionally, the morphology of the fracture surfaces and the primary failure mechanisms were analyzed using a Hirox HR-5000 3D optical microscope (Tokyo, Japan) and a Hitachi Jeol JSM-5310 scanning electron microscope (SEM).

3. Results

The microstructure of the as-built crank arms for the tested material conditions is presented in Figure 6a. This figure illustrates the main features of the as-built (AB) condition. Overall, this material condition exhibits a supersaturated Si cellular-dendritic microstructure, where aluminum is surrounded by a fibrous network of silicon. This outcome has already been confirmed in a previous study by the authors [19] and by other research teams [20]. The low-temperature stress-relieving heat treatment strategy (HT) did not introduce macroscopic alterations due to the moderately low thermal exposure, keeping the cellular substructure of the AB condition (Figure 6b). However, the high supersaturation of Si and Mg atoms in the Al lattice led to the development and coarsening of β-Mg_2Si forerunner phases (red arrows) and Si precipitates inside the α-Al cells, compared to the microstructure observed in as-build samples [21–23]. The EDX map of Al, Si, and Mg

elements (Figure 6c) showed the main alloy element distribution that verified a similar distribution in both cases.

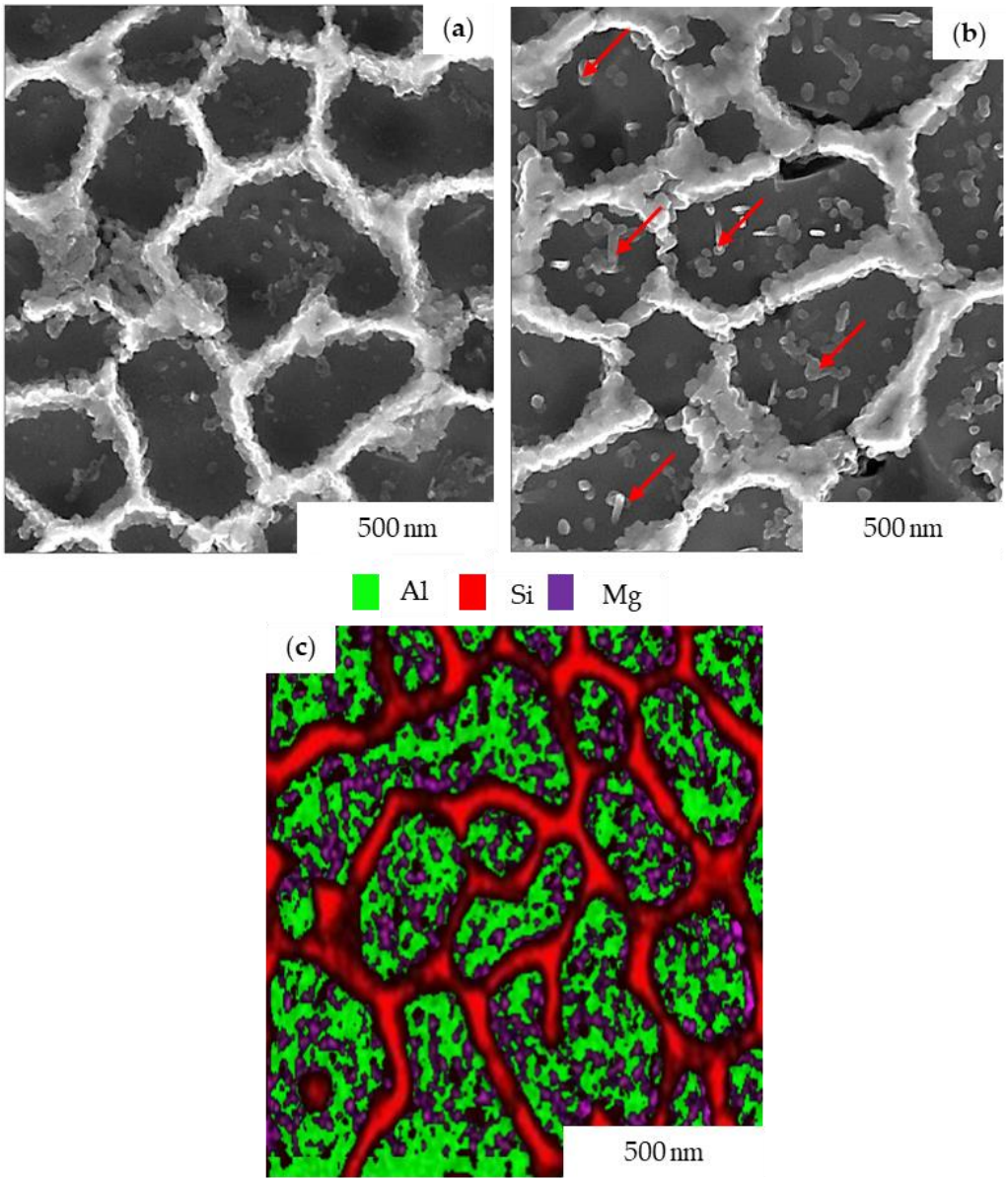

Figure 6. SEM and EDX images of the cellular structure in transversal cross-section: As-build condition (**a**,**b**) heat-treated condition, (**c**) EDX map of Al, Si, and Mg elements.

The previously described morphological modifications can be associated with a decrease in hardness in the HT condition compared to the AB condition. For the AB crank arms, the average hardness was $HV_{0.1}$ = 165.6, while for the HT ones, the average hardness value was $HV_{0.1}$ = 115.3. These values represent a decrease of approximately 30% compared to the AB condition, similar to the results presented in [4]. As a result of this reduction in hardness, lower monotonic tensile properties were observed, along with increased ductility in the heat-treated condition. Table 2 summarizes the related mechanical properties [9].

Regarding the fatigue results, three crank arms from each condition were tested, and it was verified that three of the as-build crank arms failed in the region where the maximum load was achieved in the FEA (see Figure 3). They failed before reaching the target of 100,000 cycles, being 94,312 the highest number of cycles achieved. In contrast, all the heat-

treated crank arms managed to reach 100,000 loading cycles without fracturing. Table 4 can be consulted as a resume of fatigue tests.

Table 4. Fatigue tests resume.

Condition	Standard Requirements (Number of Cycles)	Number of Cycles	Number of Cycles	Number of Cycles	Load (N)	Requirements Achieved
As-build	100,000	65,924	73,312	94,312	1300	No
HT	100,000	100,000 (without fail)	100,000 (without fail)	125,549	1300	Yes

Concerning the fractography analysis, Figure 7 shows a macrograph highlighting the crack initiation zone in the as-built crank arms. The crack initiation occurred in the same region where the maximum stress was achieved in the FEA (see Figure 3).

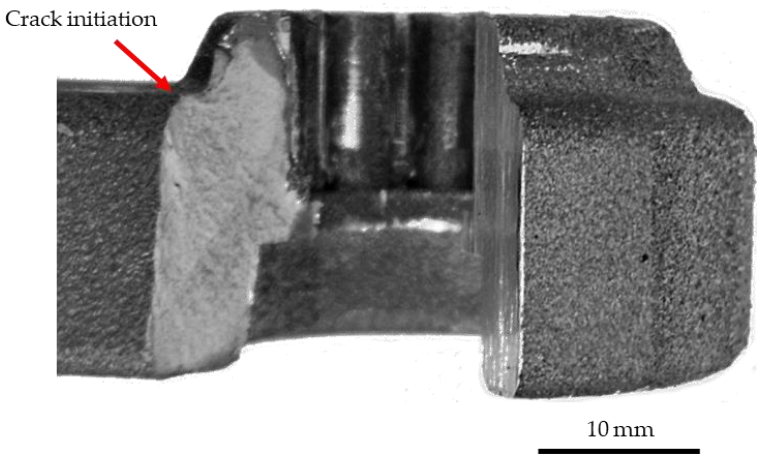

Figure 7. Crack initiation position in the as-built crank arm.

Figure 8 displays an image from the normal plane of the crack initiation and propagation regions. In this figure, the crack initiation zone and the entire crack growth region can be observed up to the fragile fracture (blue arrows).

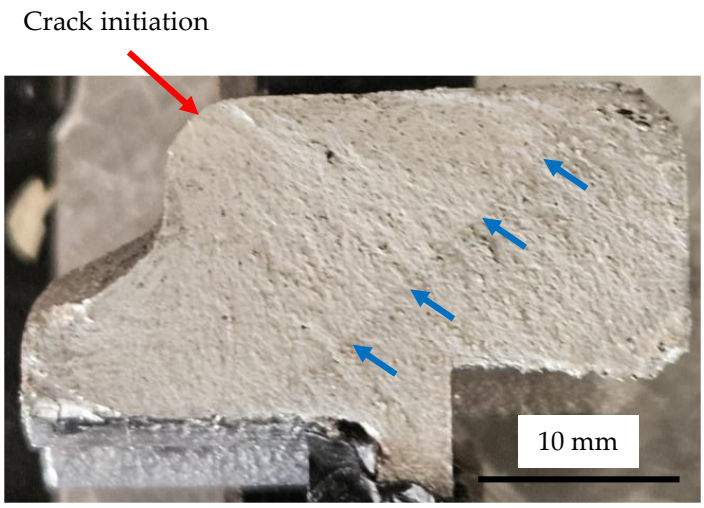

Figure 8. Crack initiation zone and crack growth region of the fractured as-built crank arm.

A detailed observation of the SEM images presented in Figure 9a,b clearly shows that the crack initiation was localized in a superficial porosity; these are representative of both cases (as-build and HT). In Figure 9b, unfused particles (blue arrow) and internal porosities (yellow arrows) can also be observed. These defects are very common in the L-PBF process, especially when it is applied to aluminum alloys [24].

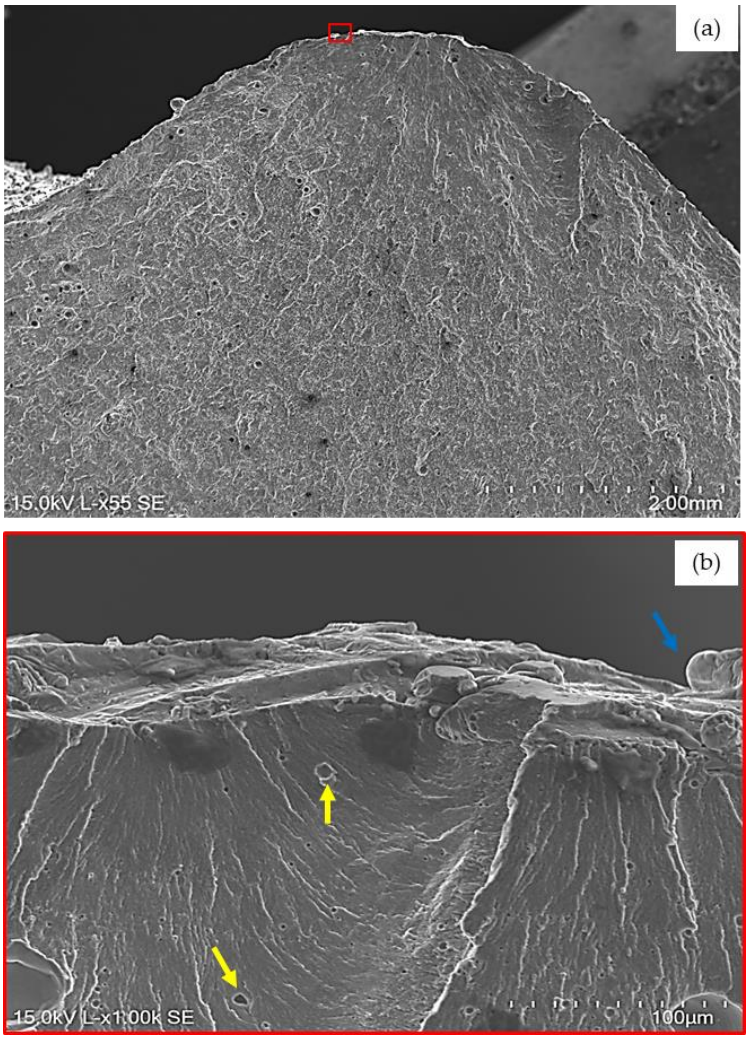

Figure 9. (**a**) Crack initiation position and (**b**) Magnification of crack initiation position (porosity).

Figure 10 presents a comparison between the fracture surfaces of a non-heat-treated crank arm that reached 94,312 fatigue life cycles and a heat-treated one that reached 125,549 fatigue life cycles. This figure shows clearly that the crack initiation position was similar in both cases, with the crack initiation location being where the stresses are highest, as previously described. In a direct comparison, it can be stated that the heat treatment increased the fatigue life by 33%, at least due to less sensitivity to defects and surface roughness obtained with the heat treatment. Materials with high hardness, such as the as-build in this case, tend to exhibit greater notch sensitivity. This is because their limited capacity for plastic deformation prevents the redistribution of concentrated stresses in the superficial defects. As a result, cracks initiated at superficial defects rapidly, leading to material failure. In contrast, the HT series showed lower hardness but greater ductility, demonstrating reduced notch sensitivity. Their ability to undergo plastic deformation allows stresses to be redistributed around superficial imperfections, increasing the fatigue life [9].

The area of the fracture surface can provide clues about the stress distribution and the presence of critical defects. For instance, a larger fracture area suggests higher stress concentrations or more significant defects, leading to reduced fatigue life, as can be verified in the as-build series [25].

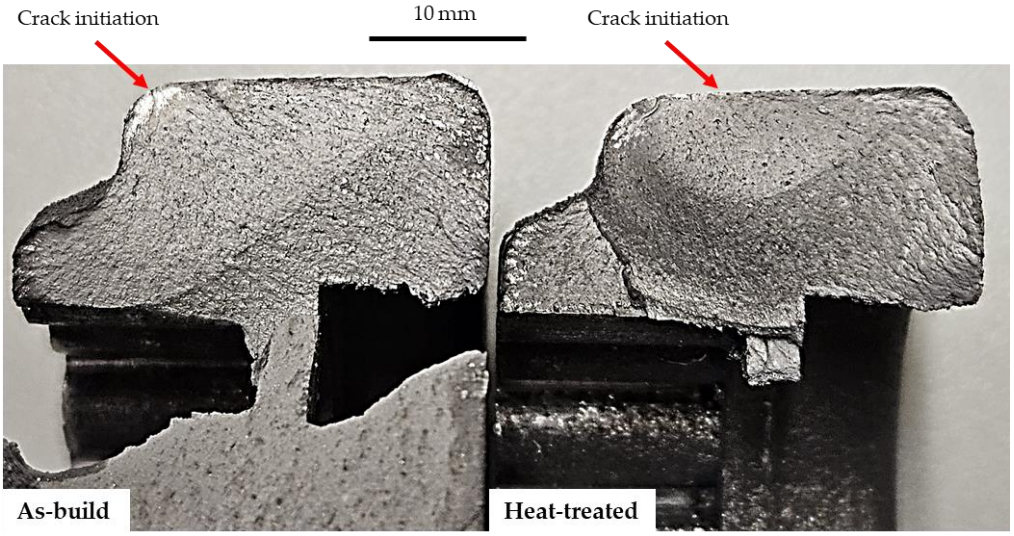

Figure 10. Crack initiation position in the as-built and heat-treated crank arms.

4. Discussion

L-PBF is a highly advanced metal additive manufacturing technology used to produce complex metallic components layer by layer that have a fine microstructure due to the rapid cooling rates involved in the process. Despite its advantages, including the ability to create intricate geometries and reduced material waste, L-PBF is susceptible to certain defects, such as porosity and surface roughness, which can significantly affect the fatigue life of components [26].

Drawing a parallel with this study, the L-PBF process produces a fine cellular-dendritic microstructure, resulting in increased strength compared to cast material, as confirmed by Krochmal et al. [3]. However, the application of the heat treatment led to the coarsening of the Si-network and partial Si precipitation within the α-Al cells, which reduced the mechanical properties of the alloy. The coarser Si network and partial Si precipitation weakened the grain boundary, solid solution, and dislocation strengthening mechanisms. Although some improvement from precipitation strengthening was expected, its effect was marginal compared to the overall reduction in other strengthening mechanisms, as observed by Chen et al. [21].

The process-induced defects introduce stress concentrators, which lead to premature crack initiation and growth, ultimately reducing the overall fatigue resistance of the material. Porosity refers to the presence of small voids or cavities within the material. In L-PBF, these voids typically form due to incomplete melting, trapped gas, or unstable melt pools. Porosity in L-PBFed parts can be categorized into two types: gas-induced porosity and lack-of-fusion porosity [27].

Gas-induced porosity occurs when inert gases such as argon or nitrogen, used in the L-PBF process or hydrogen of atmospheric air, become trapped within the melt pool and form gas pockets upon solidification. These usually present a spherical shape. Lack-of-fusion porosity, on the other hand, results from insufficient energy input, causing poor fusion between successive layers or adjacent powder particles. These pores are irregular and often more detrimental due to their sharp crack-like shapes. In terms of fatigue performance,

porosity acts as a stress concentrator, where local stresses significantly exceed the average applied stress [28].

Under cyclic loading, these stress concentrations become sites for fatigue crack initiation. Once a crack initiates at a pore, it can propagate rapidly under repeated loading, reducing the component's fatigue life. The larger the pore size and the closer the pores are to the surface, the more severe their impact on fatigue life. Pores near the surface are especially critical due to the free surface effect, which causes higher stress concentrations [29]. This issue is particularly problematic in high-cycle fatigue (HCF) regimes, where the component is subjected to a large number of stress cycles at relatively low-stress amplitudes. In such cases, fatigue life is heavily dependent on the initiation phase, and rough surfaces lead to rapid crack initiation due to the localized stress concentration.

As shown in Figure 9, the presence of pores, mainly gas-induced porosity, and the surface roughness have contributed to an early failure of the crank arm. The combined presence of porosity and surface roughness due to unfused particles in L-PBF components creates a compounding effect that further shortens fatigue life. Porosity located near the surface exacerbates the impact of surface roughness by introducing larger and deeper stress concentrators.

On the other hand, the heat treatment allowed the crank arm to reach 100,000 cycles, which can be attributed to the reduced sensitivity of the heat-treated condition to micro-notches (defects), as already confirmed by Fernandes et al. [12]. This improvement is linked to the stabilized residual stress gradient, averaging 47 MPa, compared to the as-built condition, which exhibited an increasing linear gradient from 55 to 138 MPa.

Residual stresses are well known to have a detrimental effect on fatigue life when aligned with the loading direction and have the same sign. The residual stresses act as a mean stress, raising the overall stress level during cyclic loading, which consequently reduces fatigue life and the material's resistance to crack initiation and fatigue crack growth.

In contrast, when the residual stress field is minimized or eliminated, as achieved through heat treatment in this work, the mean stress value during cyclic loading decreases. This leads to slower fatigue crack growth rates and longer crack initiation periods. Therefore, the heat treatment led to a greater tolerance of the aforementioned defects due to the reduction of the residual stress field.

5. Conclusions

Defects such as porosity and surface roughness significantly impact the fatigue life of components produced by L-PBF. Porosity acts as a stress concentrator that accelerates crack initiation and promotes early fatigue failure by increasing stress concentrations on the component's surface. This work demonstrated the benefits of applying a low-temperature stress relief heat treatment to an AlSi10Mg bicycle crank arm produced using the Laser Powder Bed Fusion technique.

The post-processed crank arm showed improved fatigue life, successfully reaching 100,000 cycles, while the as-built condition failed prematurely. The heat treatment reduced residual stresses, resulting in less sensitivity to defects and surface roughness and leading to a more stable performance under cyclic loading.

Author Contributions: M.A.: data curation, experimental tests, writing original draft, investigation. R.F.: data curation, experimental tests, writing original draft, investigation. J.d.J.: Methodology, investigation, data curation, formal analysis, validation, writing—original draft. L.B.: Funding acquisition, methodology, supervision, validation, review original draft. R.B.: formal analysis, validation, and review of the original draft. J.d.C.: Methodology, Supervision, validation. J.F.: Funding acquisition, supervisor. All authors have read and agreed to the published version of the manuscript.

Funding: This study was funded by national funds through FCT—Fundação para a Ciência e a Tecnologia, under the project UIDB/00285/2020 and LA/P/0112/2020. This research was funded by the FACI-2023-MPR-04-014323 project, supported by European Funds, and facilitated by Agência Nacional Inovação (ANI) under the Eureka smart label S0612-BRACER. This research was also funded by project MATEL, with the reference COMPETE2030-FEDER-00587200, supported by European Funds under Portugal 2030, Compete2030, and FEDER. Rui Fernandes is also grateful to the FCT for the PhD grant with reference 2022.14234.BD.

Institutional Review Board Statement: Not applicable.

Informed Consent Statement: Not applicable.

Data Availability Statement: The data presented in this study are available on request from the corresponding author. The data are not publicly available due to privacy.

Conflicts of Interest: The authors declare no conflicts of interest.

References

1. Yadroitsev, I.; Du Plessis, A.; Yadroitsava, I. Basics of Laser Powder Bed Fusion. In *Fundamentals of Laser Powder Bed Fusion of Metals*; Additive Manufacturing Materials and Technologies; Elsevier: Amsterdam, The Netherlands, 2021; pp. 15–38. [CrossRef]
2. Wu, J.; Wang, X.Q.; Wang, W.; Attallah, M.M.; Loretto, M.H. Microstructure and Strength of Selectively Laser Melted AlSi10Mg. *Acta Mater.* **2016**, *117*, 311–320. [CrossRef]
3. Krochmal, M.; Rajan, A.N.R.; Moeini, G. Microstructural and mechanical properties of AlSi10Mg: Hybrid welding of additively manufactured and cast parts. *J. Mater. Res.* **2023**, *38*, 297–311. [CrossRef]
4. Wei, P.; Wei, Z.; Chen, Z.; Du, J.; He, Y.; Li, J.; Zhou, Y. The AlSi10Mg samples produced by selective laser melting: Single track, densification, microstructure and mechanical behavior. *Appl. Surf. Sci.* **2017**, *408*, 38–50. [CrossRef]
5. Delahaye, J.; Tchoufang Tchuindjang, J.; Lecomte-Beckers, J.; Rigo, O.; Habraken, A.M.; Mertens, A. Influence of Si precipitates on fracture mechanisms of AlSi10Mg parts processed by Selective Laser Melting. *Acta Mater.* **2019**, *175*, 160–170. [CrossRef]
6. Zhou, L.; Mehta, A.; Schulz, E.; McWilliams, B.; Cho, K.; Sohn, Y. Microstructure, precipitates and hardness of selectively laser melted AlSi10Mg alloy before and after heat treatment. *Mater. Charact.* **2018**, *143*, 5–17. [CrossRef]
7. Casati, R.; Nasab, M.H.; Coduri, M.; Tirelli, V.; Vedani, M. Effects of Platform Pre-Heating and Thermal-Treatment Strategies on Properties of AlSi10Mg Alloy Processed by Selective Laser Melting. *Metals* **2018**, *8*, 954. [CrossRef]
8. Jiang, Z.; Sun, J.; Berto, F. Fatigue and Fracture Behavior of AlSi10Mg Manufactured by Selective Laser Melting: A Review. *Phys. Mesomech.* **2023**, *26*, 367–390. [CrossRef]
9. Fernandes, R.F.; Jesus, J.S.; Borrego, L.P.; Ferreira, J.A.M.; Branco, R.; Costa, J.D.; Batista, A.C.; Marques, M.J. Failure analysis of fatigue crack propagation in specimens of AlSi10Mg aluminum alloy produced by L-PBF: Effect of different heat treatments. *Eng. Fail. Anal. 163 Part B* **2024**, *163*, 108595. [CrossRef]
10. Egger, C.; Grünbart, F.; Silvayeh, Z.; Šulcová, O.; Seper, C.; Pfeifer, T.; Sommitsch, C.; Domitner, J. Mechanical Properties of Selective Laser-Melted Components of Alsi10mg for Prototype Vehicles. *Mater. Sci. Forum* **2021**, *1016*, 399–406. [CrossRef]
11. Branco, M.; Augusto, F.; de Castro, P. *Fadiga de Estruturas Soldadas*, 4th ed.; Fundação Calouste Gulbenkian: Lisabon, Portugal, 2006.
12. Fernandes, R.F.; Jesus, J.S.; Borrego, L.; Ferreira, J.A.M.; Neto, D.; Branco, R.; Costa, J.D. Notch sensitivity and heat treatment effect on the fatigue behaviour of AlSi10Mg aluminium alloy processed by additive manufacturing. *Theor. Appl. Fract. Mech.* **2024**, *133*, 104553. [CrossRef]
13. Ismail, A.Y.; Na, G.; Koo, B. Topology and Response Surface Optimization of a Bicycle Crank Arm with Multiple Load Cases. *Appl. Sci.* **2020**, *10*, 2201. [CrossRef]
14. *BS EN 573-3*; Aluminium and Aluminium Alloys—Chemical Composition and Form of Wrought Products—Chemical Composition and Form of Products. CENELEC: Brussels, Belgium, 2009.
15. *NP EN ISO 4210-8*; Cycles—Safety Requirements for Bicycles—Part 8: Pedal and Drive System Test Methods. CENELEC: Brussels, Belgium, 2019.
16. *DIN EN 1706*; Aluminium and Aluminium Alloys—Castings—Chemical Composition and Mechanical Properties. CENELEC: Brussels, Belgium, 2021.
17. *E3—11R17*; Standard Guide for Preparation of Metallographic Specimens. ASTM International: West Conshohocken, PA, USA, 2017. Available online: https://www.astm.org/e0003-11r17.html (accessed on 23 January 2024).
18. *E384—22*; Standard Test Method for Microindentation Hardness of Materials. ASTM International: West Conshohocken, PA, USA, 2022. Available online: https://www.astm.org/e0384-22.html (accessed on 23 January 2024).

19. Fernandes, R.F.; Jesus, J.S.; Branco, R.; Borrego, L.P.; Costa, J.D.; Ferreira, J.A.M. Influence of post-processing heat treatment on the cyclic deformation behaviour of AlSi10Mg aluminium alloy subjected to laser powder bed fusion. *Int. J. Fat.* **2022**, *164*, 107157. [CrossRef]
20. Liu, X.; Zhao, C.; Zhou, X.; Shen, Z.; Liu, W. Microstructure of selective laser melted AlSi10Mg alloy. *Mater. Des.* **2019**, *168*, 107677. [CrossRef]
21. Chen, S.; Tan, Q.; Gao, W.; Wu, G.; Fan, J.; Feng, Z.; Huang, T.; Godfrey, A.W.; Zhang, M.; Huang, X. Effect of heat treatment on the anisotropy in mechanical properties of selective laser melted AlSi10Mg. *Mater. Sci. Eng. A* **2022**, *858*, 144130. [CrossRef]
22. Sathishkumar, A.; Soundararajan, R.; Sivasankaran, S. Effect of Direct Aging on the Microstructure and Mechanical Behavior of AlSi10Mg Alloy: Casting Versus Selective Laser Melting. *J. Mater. Eng. Perform.* **2023**, *32*, 3215–3229. [CrossRef]
23. Di Egidio, G.; Martini, C.; Börjesson, J.; Ghassemali, E.; Ceschini, L.; Morri, A. Influence of Microstructure on Fracture Mechanisms of the Heat-Treated AlSi10Mg Alloy Produced by Laser-Based Powder Bed Fusion. *Materials* **2023**, *16*, 2006. [CrossRef]
24. Lehner, P.; Blinn, B.; Beck, T. Improving the Defect Tolerance and Fatigue Strength of AM AlSi10Mg. *Adv. Eng. Mater.* **2023**, *25*, 2201855. [CrossRef]
25. Rautio, T.; Jaskari, M.; Hietala, M.; Mustakangas, A.; Järvenpää, A. Mechanical Characterization and Fatigue Behavior of AlSi10Mg Alloy Fabricated via Laser Powder Bed Fusion: Influence of Printing Orientation. *Adv. Sci. Technol.* **2024**, *157*, 41–47. [CrossRef]
26. Armstrong, M.; Mehrabi, H.; Naveed, N. An Overview of Modern Metal Additive Manufacturing Technology. *J. Manuf. Process* **2022**, *84*, 1001–1029. [CrossRef]
27. Chu, F.; Li, E.; Shen, H.; Chen, Z.; Li, Y.; Liu, H.; Min, S.; Tian, X.; Zhang, K.; Zhou, Z.; et al. Influence of Powder Size on Defect Generation in Laser Powder Bed Fusion of AlSi10Mg Alloy. *J. Manuf. Process* **2023**, *94*, 183–195. [CrossRef]
28. Oliveira, J.P.; LaLonde, A.D.; Ma, J. Processing Parameters in Laser Powder Bed Fusion Metal Additive Manufacturing. *Mater. Des.* **2020**, *193*, 108762. [CrossRef]
29. Afroz, L.; Inverarity, S.B.; Qian, M.; Easton, M.; Das, R. Analysing the Effect of Defects on Stress Concentration and Fatigue Life of L-PBF AlSi10Mg Alloy Using Finite Element Modelling. *Prog. Addit. Manuf.* **2024**, *9*, 341–359. [CrossRef]

Disclaimer/Publisher's Note: The statements, opinions and data contained in all publications are solely those of the individual author(s) and contributor(s) and not of MDPI and/or the editor(s). MDPI and/or the editor(s) disclaim responsibility for any injury to people or property resulting from any ideas, methods, instructions or products referred to in the content.